Proximity spin-orbit coupling in a small-diameter armchair carbon nanotube on monolayer bismuthene

Marcin Kurpas*
Institute of Physics, University of Silesia in Katowice, 41-500 Chorzów, Poland

(Received 19 May 2023; revised 5 October 2023; accepted 17 October 2023; published 8 November 2023)

We study the spin-orbit proximity effects in a hybrid heterostructure built from a one-dimensional (1D) armchair carbon nanotube and two-dimensional (2D) buckled monolayer bismuthene. We show, by performing first-principles calculations, that Dirac electrons in the nanotube exhibit large spin-orbit coupling due to the close vicinity of bismuthene. The calculated low-energy band structure and the spin texture of the proximitized nanotube display a strong dependence on the position of the nanotube on the substrate, similar to the twist-angle dependence found in 2D heterostructures. Based on the first-principles results, we formulate an effective low-energy Hamiltonian of the nanotube, and we identify key interactions governing the proximity spin-orbit coupling. The proximity-induced spin splitting of Dirac cone bands is in the meV range, confirming an efficient transfer of spin-orbit coupling from bismuthene to the nanotube.

DOI: 10.1103/PhysRevB.108.195408

I. INTRODUCTION

Two-dimensional (2D) Van der Waals heterostructures have become versatile platforms to study physical phenomena in low dimensions and promising building blocks for novel devices for quantum technologies [1–3]. This was possible thanks to the great ease of modifying their electronic properties, for example by the proximity effect. It allows a material to acquire new properties by stacking it on top of another material, being the donor of those properties. Graphene, for instance, is essentially free of intrinsic spin-orbit coupling [4,5], but it can realize spin Hall states when embedded into a heterostructure with WS_2 or MoS_2 [6–9].

The effectiveness of the proximity effect is dictated largely by symmetry and physics at the interface between materials. The presence of a substrate breaks most symmetries of the host material, releasing several constraints on the electron spin and symmetry-allowed spin-orbit terms. Broken space inversion symmetry leads to the emergence of Bychkov-Rashba spin-orbit coupling affecting both the spin splitting and spin texture of Bloch states [7,10,11]. Other symmetries, such as in-plane mirror symmetry or pseudospin (sublattice) symmetry, can also be broken if present, enabling additional matrix elements of the spin-orbit Hamiltonian [12–14].

The extent to which broken symmetry affects the electronic states depends on the amplitudes of new symmetry-allowed terms. These amplitudes result from the interface crystal potential, which reflects mutual interactions and the atomic arrangement of the host material and the substrate. In commensurate 2D heterostructures, the interface potential is lattice periodic, with the period of the supercell. Within the supercell, its shape depends on the misfit and mutual arrangement of materials composing the heterostructure. The latter can be tuned, for example, by a twist angle, giving the control over the proximity effect [15–17].

When the host 2D material is replaced by a one-dimensional (1D) carbon nanotube, the 2D in-plane periodicity of the interface is preserved only in one direction, say z [see Fig. 1(c)], while in the other [y in Fig. 1(c)] it is broken due to the finite diameter of the nanotube. It has severe consequences for the electronic states in the nanotube. First, broken rotational symmetry of the nanotube does not protect the longitudinal (along the nanotube axis) component of the electron spin [18,19]. Second, a rapid variation of the crystal potential in the y direction and the nonuniform distance of carbon atoms to the substrate make room for new interface effects that are absent in flat 2D systems [20].

In this paper, we study such effects in an example hybrid 1D/2D heterostructure made of a (4,4) armchair carbon nanotube and buckled monolayer bismuthene [21–24]. Graphene-like monolayer bismuthene is a semiconductor with a direct band gap varying between 0.5 and 0.8 eV [24,25]. Strong spin-orbit coupling in bismuthene grown on Si(0001) [26] and Ag(111) [27] has been proven by spectroscopic evidence of the quantum spin Hall phase [28,29], which makes monolayer bismuth a good candidate for donor spin-orbit coupling in Van der Waals heterostructures.

To accurately describe structural changes and interactions between the nanotube and bismuthene monolayer, we approach the problem on the atomistic level and perform first-principles calculations based on the density functional theory. We show that orbital and spin-orbital properties of the nanotube are very sensitive to the position of the nanotube on the substrate. By moving the nanotube, we induce qualitative changes in the topology and spin structure of the Dirac cone bands. Specifically, we can switch between vertical spin splitting of Dirac bands characterized by a strong asymmetry between right- and left-movers, and a horizontal shift of Bloch states in crystal momentum which splits the Dirac cone

*marcin.kurpas@us.edu.pl

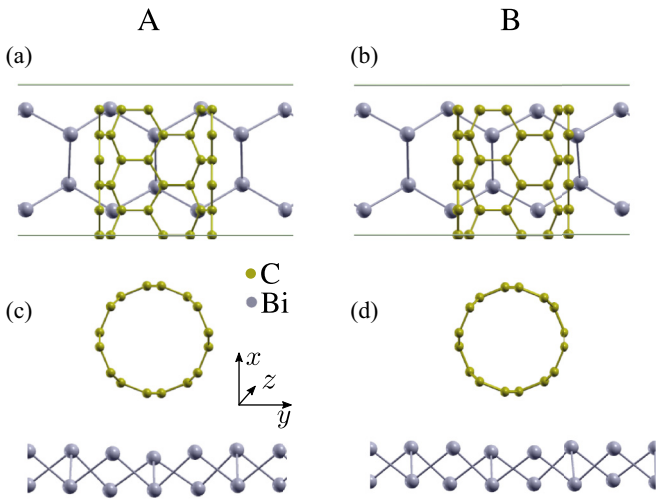

FIG. 1. Schematics of the simulated system: a metallic armchair (4,4) carbon nanotube is placed on monolayer buckled bismuthene. Depending of the position of the nanotube on bismuthene, two different configurations are realized: (a) the zigzag chain of the nanotube is in line with Bi atoms (this is labeled as the A configuration); and (b) the nanotube's bottom zigzag chain is located between two Bi atoms (B configuration). For better visibility, only C atoms closest to the substrate are drawn in (a) and (b). In (c) and (d), optimized crystal structures are shown.

into two copies of similar energy. In the latter, Bloch states are perfectly spin-polarized, creating optimal conditions for coherent spin transport in the carbon nanotube.

The band-structure topologies of the proximitized nanotube resemble those of armchair carbon nanotubes in coexisting external electric and magnetic fields [19]. We use this resemblance to develop an effective low-energy Hamiltonian of the nanotube. With its help, we identify essential spin-orbit fields responsible for the observed effects.

Proximity effects in carbon nanotubes have not yet been studied intensively. So far the focus has been on superconductivity [30], charge transfer and contact formation between nanotubes and metal surfaces [20,31–34], or optical properties of the CNT/GeSe heterostructure [35]. Carbon nanotubes proximitized to a superconductor have also been investigated in the context of topological states [36–39], but without studying the underlying proximity mechanism. Not much is known about the spin properties of nanotubes combined with 2D materials or bulk surfaces. This work provides insight into this topic and demonstrates that hybrid 1D/2D heterostructures are an attractive platform for exploring spin-orbit proximity effects, but also for spintronics applications.

The paper is organized as follows. In the next section we briefly describe the methodology and details of first-principles calculations. In Sec. III we present and discuss results of the calculations, and we develop an effective low-energy Hamiltonian for the nanotube. Section IV contains a summary and conclusions.

II. METHODS

First-principles calculations were performed with the plane-wave software package QUANTUM ESPRESSO [40,41]. The heterostructure of CNT and bismuthene was made of 24 Bi atoms building the substrate of width 25.5 Å and 48 C atoms forming three unit cells of the (4,4) armchair nanotube. The big width of bismuthene stripe was necessary to eliminate possible bending of bismuthene at the edges of the simulation cell. To ensure the commensurability of the structure, the lattice constant of bismuthene was reduced to $a_{\mathrm{Bi}} = 4.4$ Å, resulting in its slight compression of about 3% compared to the experimental value [42]. The lattice constant of CNT was $a_{\mathrm{cnt}} = 2.46$ Å. A vacuum of 16 Å was introduced in the x direction (out of plane) to avoid fictitious interactions between periodic copies of the simulation cell.

The initial geometry of the heterostructure [Figs. 1(a) and 1(b)] was optimized by minimizing the internal forces acting on the atom using the quasi-Newton scheme, as implemented in QUANTUM ESPRESSO, and assuming ionic minimization convergence criteria: 10^{-3} Ry/bohr for internal forces and 10^{-5} Ry/bohr for the total energy. During relaxation, all atoms were free to move in all directions. Taking into account that Bi is a heavy element, we performed optimization independently for the nonrelativistic and relativistic calculations, taking the output from the nonrelativistic case as the initial structure for the relativistic calculation. Nevertheless, we have not found substantial differences between the two optimized structures. In both cases, the ultrasoft pseudopotentials implementing the Perdew-Burke-Ernzerhof (PBE) [43] version of the generalized gradient approximation (GGA) exchange-correlation functional was used, with a kinetic energy cutoff of the plane wave basis sets of 48 Ry for the wave function and 485 Ry for charge density. Self-consistency was achieved with a $4 \times 10 \times 1$ Monkhorst-Pack grid [44], while for structure optimization we used a smaller grid of $1 \times 4 \times 1$. All calculations were done including the semiempirical van der Waals corrections [45,46] and the dipole correction [47] for a proper determination of the possible energy offset.

For visualization of crystal structures, we used the XCrysDen software [48]. Fitting of the model Hamiltonian to DFT data was done with the help of the least-squares fitting method implemented in the LMFIT library [49].

III. RESULTS AND DISCUSSION

A. First-principles results

We begin by discussing the geometry of the nanotube/bismuthene heterostructure. In Figs. 1(a) and 1(b) we show two configurations studied in this paper. The structures differ in the alignment of the nanotube with respect to the substrate. In configuration A, the lowest zigzag chain of the CNT is in line with the underlying Bi atoms, and C atoms closest to the substrate sit on top of Bi atoms (top position). Configuration B is made from A by shifting the nanotube in the y direction by half of the unit cell of bismuthene, such that the lowest zigzag chain of C atoms lies between Bi atoms (hollow position).

Different initial conditions for A and B setups lead to slightly different responses of bismuthene substrate during structure optimization. In case A, only the atomic Bi chain below the nanotube is pushed down, while in case B, two Bi chains lower their initial position [Figs. 1(c) and 1(d)]. The distances between the nanotube and the underneath Bi

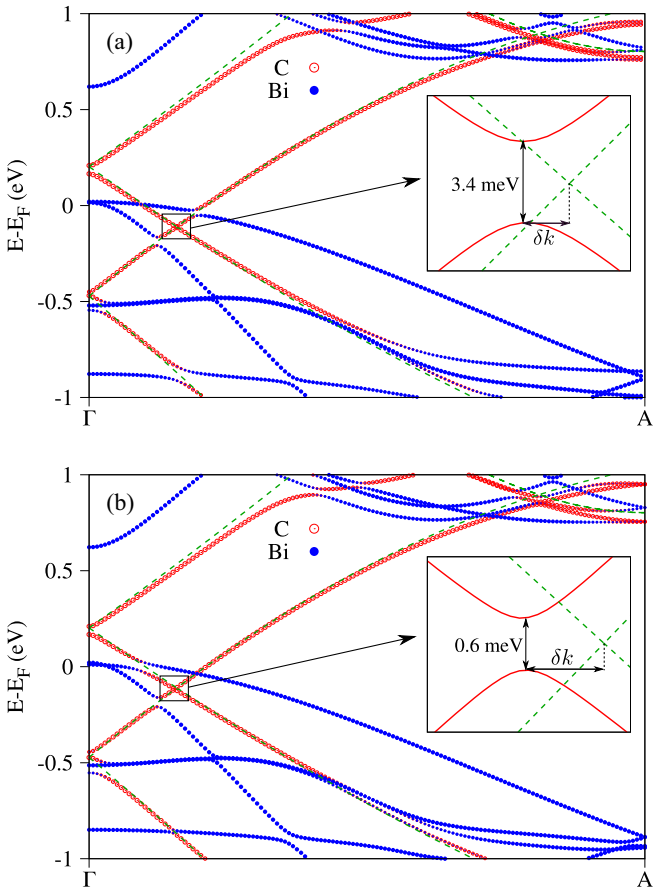

FIG. 2. Nonrelativistic band structure from first principles. (a) Band structure for the full first Brillouin zone of the nanotube and A configuration. Red represents C electrons, blue denotes Bi electrons. The band structure of pristine (4,4) CNT is plotted with the green line. The inset is a zoom at the region around the Dirac cone of the nanotube; δk is the crystal momentum shift of the Dirac cone from its position for the pristine nanotube, schematically shown by the green dashed line; $\delta k_A = 0.03$ nm^{-1}. (b) Same as (a) but for B configuration; $\delta k_B = 0.14$ nm^{-1}.

atom(s) are 3.28 and 3.15 Å for the A and B configurations, respectively. We did not notice any substantial changes to the geometry of the nanotube. Energetically the two configurations are very close to each other. The total energy of the whole system for configuration B is 16 meV lower than for A, indicating that both are similarly probable for experimental realizations.

In Fig. 2(a), we show the calculated nonrelativistic band structure for the configuration A plotted along the ΓA line in the Brillouin zone of the nanotube. This direction corresponds to crystal momentum along the nanotube axis parallel to the armchair edge of bismuthene. Bands of the nanotube (red) are easily distinguishable. The Dirac cone lies 0.1 eV below the Fermi level due to electron doping from the substrate, and it is well preserved up to ±50 meV from its center. Hybridization effects are visible on the left and right sides of the Dirac cone as anticrossings between C and Bi bands. A close look at the Dirac cone [inset in Fig. 2(a)] reveals opening a sizable orbital energy gap $\Delta^{\mathrm{A}}_{\mathrm{orb}} = 3.4$ meV in the energy spectrum of

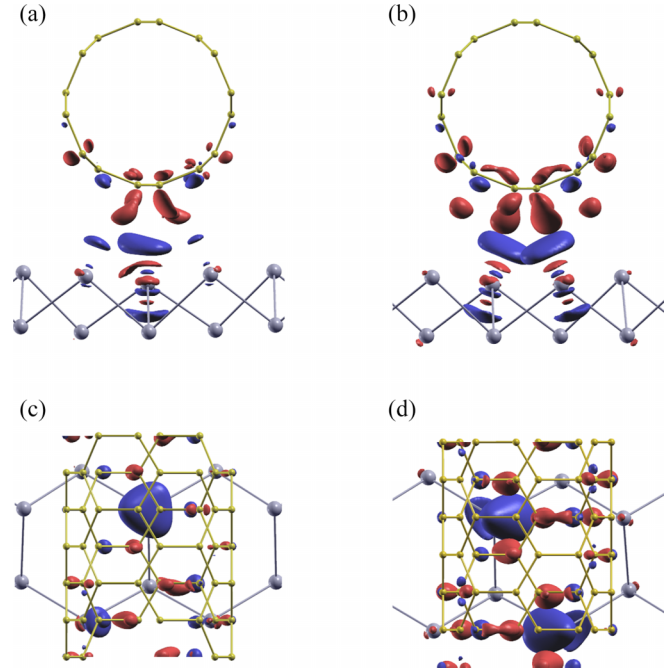

FIG. 3. Isosurfaces of charge density at the interface of CNT and bismuthene within one unit cell: (a) Side view for the configuration A; (b) side view for the configuration B. (c),(d) top view for the A and B configurations, respectively. Blue (red) represents negative (positive) values of charge density.

a metallic nanotube due to interaction with the substrate. The center of the cone is slightly shifted towards lower crystal momenta by $\delta k = 0.03$ nm^{-1} compared to the pristine nanotube.

The electronic band structure for configuration B is very similar to that of A [Fig. 2(b)]. Differences are visible in hybridization states at crystal momenta close to the position of the Dirac cone of the nanotube. The anticrossing at the Fermi energy visible to the right of the Dirac cone for A disappears and is visible to the left of the Dirac cone. A similar effect occurs at energy ≈−0.75 eV below the Fermi level. A slightly larger shift of the Dirac cone towards smaller crystal momenta, $\delta k_B = 0.14$ nm^{-1}, is observed. Most striking is the reduction of the orbital gap, $\Delta^{\mathrm{B}}_{\mathrm{orb}} = 0.6$ meV, which is almost six times less than for case A.

Since only orbital effects have been considered so far, such significant differences in Δ_{orb} between the configurations should also be visible in the interface potential. Our conjecture is confirmed in Fig. 3, where we show the interface charge density isosurfaces $\rho(\mathbf{r})_{\mathrm{int}}$,

$$\rho(\mathbf{r})_{\mathrm{int}} = \rho(\mathbf{r}) - \rho(\mathbf{r})_{\mathrm{Bi}} - \rho(\mathbf{r})_{\mathrm{cnt}}. \tag{1}$$

Here $\rho(\mathbf{r})$ is the total charge density of the full system, and $\rho(\mathbf{r})_{\mathrm{Bi/cnt}}$ is the charge density of the slab/nanotube, respectively. Qualitative differences in $\rho(\mathbf{r})_{\mathrm{int}}$ between A and B configurations are evident. For the former, a single big charge pocket [big blue blob in Fig. 3(c)] is formed (approximately) below one C atom, which leads to strong sublattice (pseudospin) symmetry breaking. For the latter, two blobs are localized below C atoms belonging to different sublattices of the nanotube [Fig. 3(d)]. Sublattice asymmetry is much

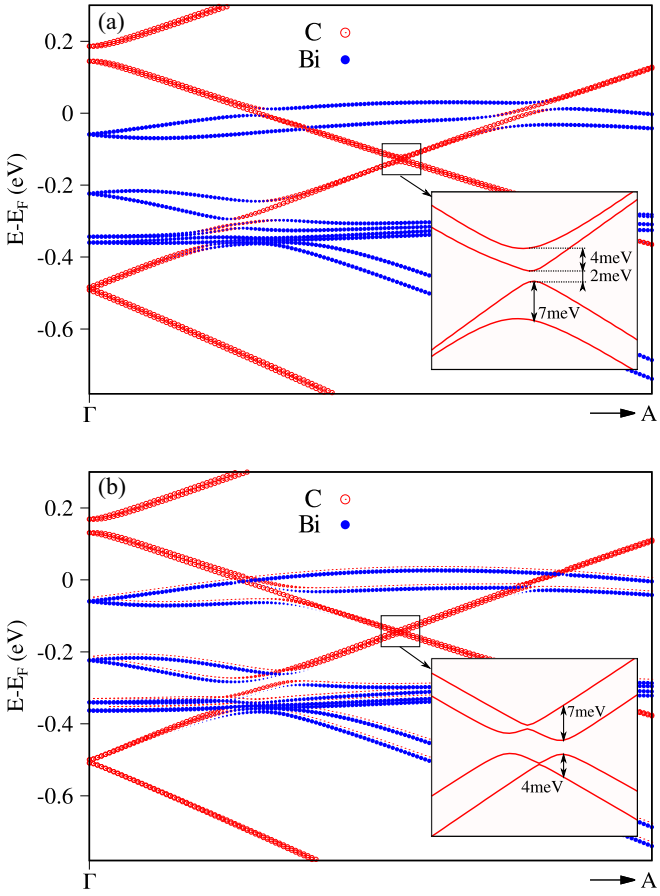

FIG. 4. Relativistic band structure from first principles projected onto C (red) and Bi (blue) atomic states. Panels (a) and (b) correspond to the A and B configurations, respectively. Strong repulsion and spin splitting in Bi bands modifies hybridization between states of CNT and bismuthene compared to the nonrelativistic calculation.

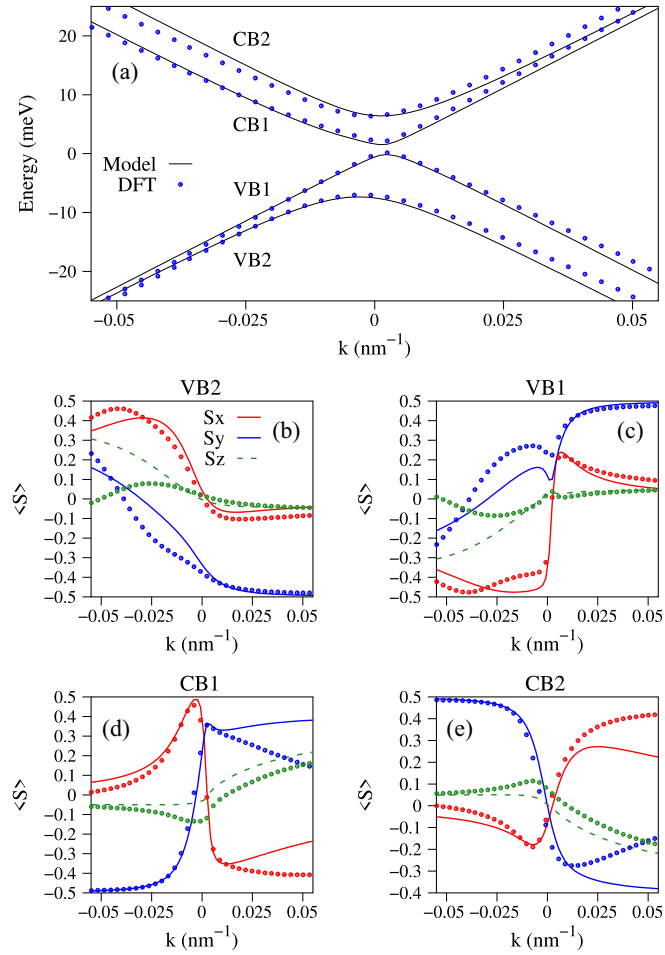

FIG. 5. Electronic properties of (4,4) armchair carbon nanotube on monolayer bismuthene for the configuration A. (a) Dirac cone bands of the nanotube; (b)–(d) corresponding spin expectation values of bands shown in (a). Dots represent first-principles data, while lines are results from the effective Hamiltonian (7).

weaker in this case, which the effective Hamiltonian analysis will further confirm.

Relativistic effects in carbon nanotubes are much stronger than in flat graphene due to curvature-induced hopping between σ and π orbitals [18,50–53]. In armchair nanotubes, the effects of intrinsic spin-orbit coupling in the band structure are manifested by opening a spin-orbital gap at the K-point, while bands remain spin doublets, which is guaranteed by space inversion and time-reversal symmetry. Theory predicts that the value of the spin-orbital gap at the Dirac point is $\Delta_{so}^{K} = 0.6\ \text{meV}/d$–$0.85\ \text{meV}/d$, where d is the diameter of the nanotube in nanometers [54,55]. This is roughly two orders larger than for graphene, for which $\Delta_{so}^{K} \approx 25\ \mu\text{eV} - 40\ \mu\text{eV}$ [4,5]. Our first-principles calculations yield for a pristine (4,4) nanotube of diameter $d = 0.55$ nm, $\Delta_{so}^{K} = 1.55$ meV, in good agreement with the above formula.

In Figs. 4(a) and 4(b), we show calculated relativistic band structures of CNT/Bi heterostructure projected onto the atomic states of Bi and C. The inclusion of SOC removes the orbital degeneracy of Bi states at the Fermi level, pulling them apart by 164 meV. Spin states are also split off by an energy of about 50 meV, which is unsurprising considering the sizable atomic number of bismuth $Z = 83$ and strong spin-orbit coupling in bismuthene [25].

Similar to the nonrelativistic case, the Dirac cone of the nanotube is well separated from Bi bands. A closer look reveals differences in the band-structure topology for A and B configurations. For the former, the top valence and bottom conduction bands of the nanotube meet at the same k-point, but the outer spin subbands are misaligned, leading to a pronounced asymmetry of spin splitting $\Delta_{\uparrow\downarrow}$ between the right and left movers [see the inset in Fig. 4(a)]. The splitting is also particle-hole asymmetric. In the hole branch, states at the band maximum are split off by $\Delta_{\uparrow\downarrow} = 7$ meV, while at the conduction-band minimum $\Delta_{\uparrow\downarrow} = 4$ meV. In both cases, the values largely exceed splittings induced by a transverse external electric field. Our first-principles calculations give splitting energy on the order $\approx 10\ \mu\text{eV/Vnm}^{-1}$, on the same level as for graphene [4].

The corresponding spin expectation values of Dirac cone bands are shown in Figs. 5(b)–5(d). In addition to the S_y component, expected from the crystal potential gradient in the x direction (normal to the surface of bismuthene), S_x

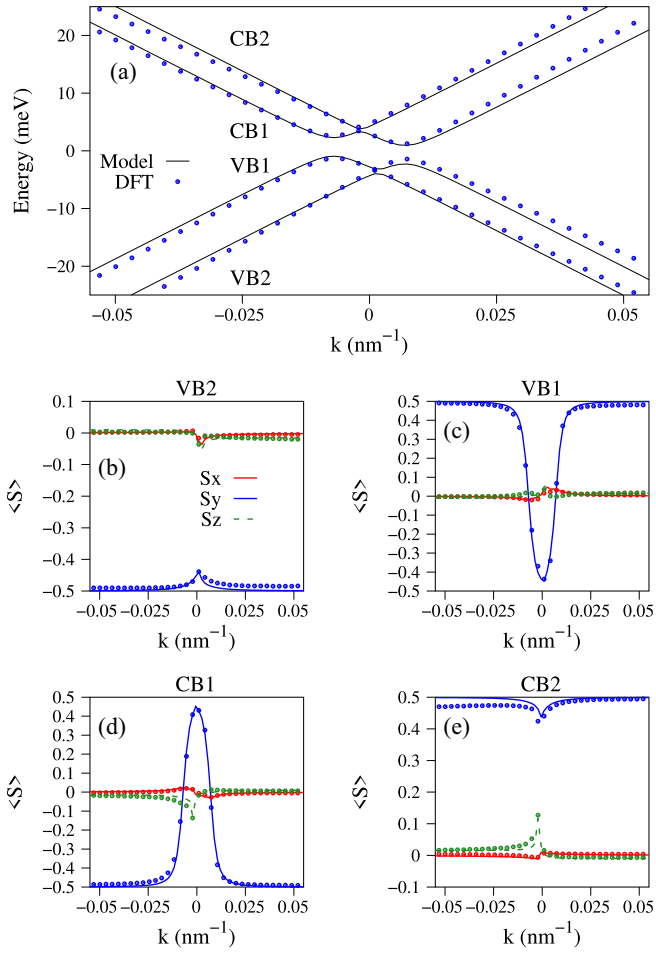

FIG. 6. Same as Fig. 5 but for the configuration B.

is also pronounced. The S_z component is weak, which can be understood as a consequence of the lack of an intrinsic Zeeman field polarizing spins along the tube axis in chiral and zigzag tubes [54]. Like the band structure, the spin texture displays an unusual asymmetry between left- and right-movers. This asymmetry can lead to anisotropic spin scattering and to asymmetric spin transmission probability under forward and reverse bias—the spin rectification effect [see Fig. 5(c)]. However, since an equivalent band structure of opposite spin polarization exists at the K' valley, the observation of such effects in the experiment would require breaking of valley symmetry.

A qualitatively different picture of the Dirac cone bands is seen for configuration B [see the inset in Fig. 4(b)]. Instead of a vertical energy splitting of spin states, we observe a horizontal shift of bands in crystal momentum, in the opposite direction for each band, resulting in two cones of similar energies but opposite spin. This is confirmed by tracing the spin texture of bands, shown in Figs. 6(b)–6(d). For instance, the spin expectation value in the band VB1 changes from 0.5 to -0.5 at the band maximum ($k \approx -0.008$ nm^{-1}), but at $k = 0$ the two cones interchange and spin turns back towards 0.5. Unlike case A, now only the S_y spin component is present, which has huge implications for spin dynamics in the nanotube. For the Fermi level lying at least 5 meV below the maximum of the lower branch of the Dirac cone (or 5 meV above the minimum of the upper branch), bands are perfectly spin-polarized and display a persistent spin texture. In this case, long spin coherence at spin diffusion lengths is expected due to the strongly suppressed Dyakonov-Perel [56,57] spin relaxation mechanism [58,59].

B. Effective Hamiltonian

The topology of Dirac cone bands is very similar to the energy spectrum of armchair nanotubes in coexisting transverse electric and magnetic fields [19,60]. We exploit these similarities to build an effective model capturing essential features shown by first-principles results. We start from the orbital Hamiltonian of an infinite pristine armchair nanotube describing the linear dispersion of the Dirac cone [19],

$$H^{\text{arm}} = \tau \hbar v_F k \sigma_2. \tag{2}$$

Here, $\tau = \pm 1$ is the valley index, v_F is the Fermi velocity, k is longitudinal crystal momentum, and σ_2 is the Pauli matrix acting on the sublattice degree of freedom. To describe the opening of the orbital gap, we introduce a staggered on-site potential Δ_{st} diagonal in spin basis,

$$H^{\text{st}} = \Delta_{\text{st}} \sigma_3. \tag{3}$$

The parameter Δ_{st} originates mainly from substrate-induced pseudospin symmetry breaking discussed in Sec. III A, but it includes the contribution from other factors affecting the orbital gap, such as the deformation of the nanotube. We use the orbital Hamiltonian $H^{\text{orb}} = H^{\text{arm}} + H^{\text{st}}$ to find initial values for v_F and Δ_{st} by fitting the model to the first-principles energy spectrum.

Next, we add the effects of spin-orbit coupling. The intrinsic spin-orbit coupling opening a spin-orbital gap at the K-point in a pristine armchair nanotube is given by [19,54]

$$H^{\text{int}} = \alpha S_z \sigma_1, \tag{4}$$

where S_z is the spin one-half operator with eigenvalues ± 1, and α is a parameter defining the strength of SOC.

The interaction of the nanotube with the substrate changes the charge density profile and generates nonvanishing crystal potential gradients, or equivalently, electric fields. A static electric field in the x (stacking) direction generates the Hamiltonian [19]

$$H^{R} = \tau E_x S_y \sigma_2, \tag{5}$$

where E_x is the electric field strength in meV. This term is responsible for symmetrically splitting spin subbands in each branch of the Dirac cone and spin polarization in the y direction.

Finally, we define the time-reversal-symmetric effective spin-orbit Hamiltonian H^{so} that, along with Eq. (5), will play the central role in reconstructing the first-principles band structure of the nanotube,

$$H^{\text{so}} = \tau \Omega_1 S_y \sigma_0 + \tau \Omega_2 S_y \sigma_3 + \Omega_3 S_y \sigma_1 + \tau \Omega_4 S_z \sigma_2. \tag{6}$$

The parameters Ω_i, $i = \{1, 2, 3, 4\}$, are amplitudes of effective spin-orbit fields. Since all symmetries of the nanotube are broken, there are no constraints on the form of terms appearing in H^{so}. Thus, any term of the product $[\boldsymbol{p} \times \nabla V(\boldsymbol{r})] \cdot \boldsymbol{\sigma}$, including

TABLE I. Parameters of the effective Hamiltonian (2) obtained by least-squares fitting to the first-principles data.

Configuration	Δ_{st} (meV)	v_F (nm s^{-1})	E_x (meV)	Ω_1 (meV)	Ω_2 (meV)	Ω_3 (meV)	Ω_4 (meV)	α (meV)
A	1.74	6.9×10^{14}	−1.75	1.4	−2.6	0	−0.3	3.2
B	0.17	6.8×10^{14}	0.67	3.2	−0.16	0.1	−0.07	1.6

H^R, is allowed, provided it does not break time-reversal symmetry. However, we kept a minimal number of possible terms allowing us to reconstruct the first-principles energy spectrum and the spin texture.

The first term in (6) can be interpreted as a Hamiltonian of an effective magnetic field in the y direction, perpendicular to the electric field E_x and to the nanotube axis (z axis). It is sublattice-even, and is similar to the Hamiltonian of the intrinsic chiral magnetic field in zigzag and chiral nanotubes, $H_Z = \tau\beta S_z\sigma_0$, where the parameter β depends on the chiral angle θ, $\beta \sim 3\theta$ [54,61]. For armchair carbon nanotubes, $\theta = \pi/6$, giving $\beta = 0$. Here, the field polarizes spins in the direction transverse to the tube axis, thus its origin is of a different nature from that of H_Z. Besides modifying the energy of spin states, already split off by the electric field E_x, this term introduces a spin-dependent shift in k, leading to an asymmetry of spin splitting for left- and right-movers (if $E_x \neq 0$).

The second term in (6) describes a staggered effective magnetic field with opposite sign on the A and B sublattices (sublattice-odd). It is analogous to the valley-Zeeman SOC in graphene with broken pseudospin symmetry [7,62], and it originates from a sublattice-dependent Kane-Mele SOC term [28]. The remaining two terms in (6) are required for correct reconstruction of spin expectation values. They involve sublattice mixing via operators σ_1 and σ_2, in contrast to Ω_1 and Ω_2, which act on a given sublattice.

The parameters of the effective model are found by least-squares fitting the full Hamiltonian

$$H = H^{\text{orb}} + H^{\text{int}} + H^R + H^{\text{so}} \tag{7}$$

to DFT data. Theoretical results superimposed on the first-principles data are shown in Figs. 5 and 6, while the corresponding parameters are collected in Table I.

The overall agreement of the model with DFT data is very good. Some discrepancies in spin texture are visible in Figs. 5(a)–5(d), showing a rather complicated nature of the induced spin-orbit coupling, probably by the nearby hybridization with the Bi bands. Looking at the values listed in Table I, it is clear that the configurations A and B activate different orbital and spin-orbital fields generated by the interface crystal potential. While for configuration A, terms with Δ_{st}, E_x, Ω_1, and Ω_2 are essential for the reconstruction of the band structure and the spin texture, for configuration B the terms with E_x and Ω_1 are sufficient to get a good agreement with DFT data. The significant value of Ω_1 in the latter case demonstrates the dominant contribution from the Zeeman-like field, which here is of an extrinsic origin.

The topologies of Dirac cone bands of the nanotube discussed above resemble those of graphene on transition-metal dichalcogenides, where the spin-orbital proximity effect was controlled by the twist angle between the components of the heterobilayers [15,17,63]. Here, a similar effect is achieved by introducing a shift instead of a twist, which was shown to have marginal effects on proximity spin-orbit coupling in 2D heterostructures [8].

C. Nonarmchair and large nanotubes

Let us now discuss how the chirality and diameter of nanotubes can influence the observed proximity effect. In contrast to armchair nanotubes, spin-orbit coupling in zigzag and chiral nanotubes is intrinsically asymmetric for electrons and holes [54,55]. The asymmetry results from different contributions of the σ electrons to the bonding and antibonding states forming the Dirac bands [55]. Bonding and antibonding states may interact with the substrate differently, giving a different response of the electron and hole branches to the proximity spin-orbit coupling. We expect, however, that in most cases the electron-hole splitting asymmetry will be reduced due to an enhancement of SOC in the branch with weaker SOC. The branch with stronger SOC will be less affected because of a comparable energy scale to the proximity spin-orbit coupling (meV).

In terms of an effective spin-orbit coupling Hamiltonian, the electron-hole asymmetry in Dirac bands is generated by the competition between the sublattice off-diagonal term, Eq. (4), and the sublattice diagonal effective Zeeman term,

$$H_Z(\theta) = \tau\beta S_z\sigma_0, \tag{8}$$

where $\beta \approx -0.31\cos(3\theta)$ meV nm$/R$ (nm) is an effective magnetic field, and θ is the chiral angle [54]. Upon decreasing the chiral angle θ, the importance of $H_Z(\theta)$ increases and the asymmetry becomes larger. In addition to contributing to electron-hole asymmetry, the effective Zeeman term plays an important role in stabilizing spin polarization of bands in the direction parallel to the nanotube axis. It is most effective for small chiral angles, when $\cos 3\theta \approx 1$. In such cases, the parallel spin component should be more prominent in the spin texture, in contrast to armchair nanotubes or chiral nanotubes with large θ, for which $\cos 3\theta \approx 0$. The effects of finite chirality should also affect the interface between the nanotube and the substrate. We expect that sublattice-dependent coupling to the substrate will be washed out by chirality, resulting in smaller Δ_{st} and band-structure asymmetry.

Apart from chirality, curvature can also affect the proximity effect in nanotubes. In small-diameter nanotubes, large curvature leads to a shift of p_z orbitals to the outside of the nanotube enhancing chemical reactivity and interaction of π orbitals with the valence states of the substrate [20,64]. As a result, the distance of the nanotube to the substrate is expected to be smaller for small nanotubes than for the large ones, increasing the hybridization effects and transfer of SOC from the substrate to the nanotube. Large curvature

of small nanotubes may also increase the role of the in-plane component of the interface crystal potential at the edges of the nanotube. Its significance should lessen as the diameter increases, eventually disappearing in the limit of flat graphene. On the other hand, the contribution of the proximity effect to overall spin-orbit coupling in the Dirac bands should be bigger for large nanotubes than for small ones due to weaker intrinsic spin-orbit coupling in the former.

IV. CONCLUSIONS

We have studied proximity spin-orbit coupling in a hybrid 1D/2D heterostructure made of a small armchair carbon nanotube and buckled monolayer bismuthene using first-principles calculations. We have found that Dirac bands of the nanotube are very sensitive to the interface crystal potential reflecting the atomic environment created by the substrate. By changing the position of the nanotube, we induced qualitative changes in the topology and spin texture of Dirac cone Bloch states. In particular, we demonstrated that a perfect spin polarization of Dirac bands can be obtained, creating optimal conditions for efficient spin transport in proximitized carbon nanotubes. By introducing a slight shift in interfacial alignment, a strong asymmetry in spin splitting and spin texture between left- and right-moving electrons can be generated, which, under breaking of valley symmetry, can lead to spin rectification. The proximity-induced spin-orbit coupling in Dirac bands is in the meV range, confirming an effective transfer of spin-orbit coupling from bismuthene to the nanotube.

The fabrication of aligned arrays of wafer-scale carbon nanotubes has long been an obstacle to applying nanotubes in microelectronics. Recent advances in the controlled growth and manipulation of single-walled carbon nanotubes [65–67] and one-dimensional nanotube-based heterostructures [68,69] are overcoming these obstacles and offer excellent prospects for practical applications of nanotubes. Our results show that with such precise positioning techniques, proximitized carbon nanotubes may be attractive systems for spintronics applications.

ACKNOWLEDGMENTS

The authors thank M. Marganska-Lyzniak, M. Gmitra, M. Milivojević, and J. Fabian for fruitful discussions. The authors acknowledge support from the Interdisciplinary Centre for Mathematical and Computational Modelling (ICM), University of Warsaw (UW), under Grant No. GA84-43. The project is cofinanced by the National Center for Research and Development (NCBR) under the V4-Japan project BGapEng V4-JAPAN/2/46/BGapEng/2022.

[1] K. S. Novoselov, A. Mishchenko, A. Carvalho, and A. H. C. Neto, Science **353**, aac9439 (2016).
[2] I. Žutić, A. Matos-Abiague, B. Scharf, H. Dery, and K. Belashchenko, Mater. Today **22**, 85 (2019).
[3] A. Avsar, H. Ochoa, F. Guinea, B. Özyilmaz, B. J. van Wees, and I. J. Vera-Marun, Rev. Mod. Phys. **92**, 021003 (2020).
[4] M. Gmitra, S. Konschuh, C. Ertler, C. Ambrosch-Draxl, and J. Fabian, Phys. Rev. B **80**, 235431 (2009).
[5] J. Sichau, M. Prada, T. Anlauf, T. J. Lyon, B. Bosnjak, L. Tiemann, and R. H. Blick, Phys. Rev. Lett. **122**, 046403 (2019).
[6] A. Avsar, J. Y. Tan, T. Taychatanapat, J. Balakrishnan, G. K. W. Koon, Y. Yeo, J. Lahiri, A. Carvalho, A. S. Rodin, E. C. T. O'Farrell, G. Eda, A. H. Castro Neto, and B. Özyilmaz, Nat. Commun. **5**, 4875 (2014).
[7] M. Gmitra and J. Fabian, Phys. Rev. B **92**, 155403 (2015).
[8] M. Gmitra, D. Kochan, P. Högl, and J. Fabian, Phys. Rev. B **93**, 155104 (2016).
[9] C. K. Safeer, J. Ingla-Aynés, F. Herling, J. H. Garcia, M. Vila, N. Ontoso, M. R. Calvo, S. Roche, L. E. Hueso, and F. Casanova, Nano Lett. **19**, 1074 (2019).
[10] Y. Bychkov and E. Rashba, Pis'ma Zh. Eksp. Teor. Fiz. **39**, 66 (1984) [JETP Lett. **39**, 78 (1984)].
[11] W. Han, R. K. Kawakami, M. Gmitra, and J. Fabian, Nat. Nanotechnol. **9**, 794 (2014).
[12] G. Giovannetti, P. A. Khomyakov, G. Brocks, P. J. Kelly, and J. van den Brink, Phys. Rev. B **76**, 073103 (2007).
[13] C. Weeks, J. Hu, J. Alicea, M. Franz, and R. Wu, Phys. Rev. X **1**, 021001 (2011).
[14] D. Kochan, S. Irmer, and J. Fabian, Phys. Rev. B **95**, 165415 (2017).
[15] Y. Li and M. Koshino, Phys. Rev. B **99**, 075438 (2019).
[16] K. Zollner, P. E. Faria Junior, and J. Fabian, Phys. Rev. B **100**, 085128 (2019).
[17] T. Naimer, K. Zollner, M. Gmitra, and J. Fabian, Phys. Rev. B **104**, 195156 (2021).
[18] D. Huertas-Hernando, F. Guinea, and A. Brataas, Phys. Rev. B **74**, 155426 (2006).
[19] J. Klinovaja, M. J. Schmidt, B. Braunecker, and D. Loss, Phys. Rev. B **84**, 085452 (2011).
[20] M. Hasegawa and K. Nishidate, Phys. Rev. B **83**, 155435 (2011).
[21] T. Nagao, J. T. Sadowski, M. Saito, S. Yaginuma, Y. Fujikawa, T. Kogure, T. Ohno, Y. Hasegawa, S. Hasegawa, and T. Sakurai, Phys. Rev. Lett. **93**, 105501 (2004).
[22] S. Yaginuma, K. Nagaoka, T. Nagao, G. Bihlmayer, Y. M. Koroteev, E. V. Chulkov, and T. Nakayama, J. Phys. Soc. Jpn. **77**, 014701 (2008).
[23] I. K. Drozdov, A. Alexandradinata, S. Jeon, S. Nadj-Perge, H. Ji, R. J. Cava, B. A. Bernevig, and A. Yazdani, Nat. Phys. **10**, 664 (2014).
[24] E. Aktürk, O. U. Aktürk, and S. Ciraci, Phys. Rev. B **94**, 014115 (2016).
[25] M. Kurpas, P. E. Faria Junior, M. Gmitra, and J. Fabian, Phys. Rev. B **100**, 125422 (2019).
[26] F. Reis, G. Li, L. Dudy, M. Bauernfeind, S. Glass, W. Hanke, R. Thomale, J. Schäfer, and R. Claessen, Science **357**, 287 (2017).
[27] S. Sun, J.-Y. You, S. Duan, J. Gou, Y. Z. Luo, W. Lin, X. Lian, T. Jin, J. Liu, Y. Huang, Y. Wang, A. T. S. Wee, Y. P. Feng, L. Shen, J. L. Zhang, J. Chen, and W. Chen, ACS Nano **16**, 1436 (2022).
[28] C. L. Kane and E. J. Mele, Phys. Rev. Lett. **95**, 226801 (2005).
[29] B. A. Bernevig and S.-C. Zhang, Phys. Rev. Lett. **96**, 106802 (2006).

[30] A. F. Morpurgo, J. Kong, C. M. Marcus, and H. Dai, Science **286**, 263 (1999).

[31] S. Okada and A. Oshiyama, Phys. Rev. Lett. **95**, 206804 (2005).

[32] Y. Takagi and S. Okada, Phys. Rev. B **84**, 035406 (2011).

[33] A. A. Kuzubov, E. A. Kovaleva, P. Avramov, A. V. Kuklin, N. S. Mikhaleva, F. N. Tomilin, S. Sakai, S. Entani, Y. Matsumoto, and H. Naramoto, J. Appl. Phys. **116**, 084309 (2014).

[34] Y. Liao, K. Mustonen, S. Tulić, V. Skákalová, S. A. Khan, P. Laiho, Q. Zhang, C. Li, M. R. Monazam, J. Kotakoski, H. Lipsanen, and E. I. Kauppinen, ACS Nano **13**, 11522 (2019).

[35] Y. Mao, Z. Guo, J. Yuan, and T. Sun, Nanomaterials **11**, 1565 (2021).

[36] R. Egger and K. Flensberg, Phys. Rev. B **85**, 235462 (2012).

[37] J. Klinovaja, S. Gangadharaiah, and D. Loss, Phys. Rev. Lett. **108**, 196804 (2012).

[38] M. Marganska, L. Milz, W. Izumida, C. Strunk, and M. Grifoni, Phys. Rev. B **97**, 075141 (2018).

[39] L. Milz, W. Izumida, M. Grifoni, and M. Marganska, Phys. Rev. B **100**, 155417 (2019).

[40] P. Giannozzi, S. Baroni, N. Bonini, M. Calandra, R. Car, C. Cavazzoni, D. Ceresoli, G. L. Chiarotti, M. Cococcioni, I. Dabo *et al.*, J. Phys.: Condens. Matter **21**, 395502 (2009).

[41] P. Giannozzi, O. Andreussi, T. Brumme, O. Bunau, M. Buongiorno Nardelli, M. Calandra, R. Car, C. Cavazzoni, D. Ceresoli, M. Cococcioni *et al.*, J. Phys.: Condens. Matter **29**, 465901 (2017).

[42] H. Mönig, J. Sun, Y. M. Koroteev, G. Bihlmayer, J. Wells, E. V. Chulkov, K. Pohl, and P. Hofmann, Phys. Rev. B **72**, 085410 (2005).

[43] J. P. Perdew, K. Burke, and M. Ernzerhof, Phys. Rev. Lett. **77**, 3865 (1996); **78**, 1396(E) (1997).

[44] H. J. Monkhorst and J. D. Pack, Phys. Rev. B **13**, 5188 (1976).

[45] S. Grimme, J. Comput. Chem. **27**, 1787 (2006).

[46] V. Barone, M. Casarin, D. Forrer, M. Pavone, M. Sambi, and A. Vittadini, J. Comput. Chem. **30**, 934 (2009).

[47] L. Bengtsson, Phys. Rev. B **59**, 12301 (1999).

[48] A. Kokalj, J. Mol. Graph. Model. **17**, 176 (1999).

[49] M. Newville, R. Otten, A. Nelson, T. Stensitzki, A. Ingargiola, D. Allan, A. Fox, F. Carter, M. R. Osborn, D. Pustakhod *et al.*, lmfit/lmfit-py: 1.1.0, Zenodo (2022).

[50] T. Ando, J. Phys. Soc. Jpn. **69**, 1757 (2000).

[51] F. Kuemmeth, S. Ilani, D. C. Ralph, and P. L. McEuen, Nature (London) **452**, 448 (2008).

[52] S. H. Jhang, M. Marganska, Y. Skourski, D. Preusche, B. Witkamp, M. Grifoni, H. van der Zant, J. Wosnitza, and C. Strunk, Phys. Rev. B **82**, 041404(R) (2010).

[53] G. A. Steele, F. Pei, E. A. Laird, J. M. Jol, H. B. Meerwaldt, and L. P. Kouwenhoven, Nat. Commun. **4**, 1573 (2013).

[54] W. Izumida, K. Sato, and R. Saito, J. Phys. Soc. Jpn. **78**, 074707 (2009).

[55] J. Zhou, Q. Liang, and J. Dong, Phys. Rev. B **79**, 195427 (2009).

[56] M. I. Dyakonov and V. I. Perel, Phys. Lett. A **35**, 459 (1971).

[57] M. I. Dyakonov and V. I. Perel, Fiz. Tverd. Tela (Leningrad) **13**, 3581 (1971) [Sov. Phys. Solid State **13**, 3023 (1971)].

[58] A. W. Holleitner, V. Sih, R. C. Myers, A. C. Gossard, and D. D. Awschalom, Phys. Rev. Lett. **97**, 036805 (2006).

[59] J. Schliemann, Rev. Mod. Phys. **89**, 011001 (2017).

[60] W. DeGottardi, T.-C. Wei, and S. Vishveshwara, Phys. Rev. B **79**, 205421 (2009).

[61] J.-S. Jeong and H.-W. Lee, Phys. Rev. B **80**, 075409 (2009).

[62] M. Gmitra, D. Kochan, and J. Fabian, Phys. Rev. Lett. **110**, 246602 (2013).

[63] A. David, P. Rakyta, A. Kormányos, and G. Burkard, Phys. Rev. B **100**, 085412 (2019).

[64] A. Maiti and A. Ricca, Chem. Phys. Lett. **395**, 7 (2004).

[65] R. Zhang, Y. Zhang, and F. Wei, Chem. Soc. Rev. **46**, 3661 (2017).

[66] M. He, S. Zhang, and J. Zhang, Chem. Rev. **120**, 12592 (2020).

[67] L. Liu, J. Han, L. Xu, J. Zhou, C. Zhao, S. Ding, H. Shi, M. Xiao, L. Ding, Z. Ma, C. Jin, Z. Zhang, and L.-M. Peng, Science **368**, 850 (2020).

[68] R. Xiang, T. Inoue, Y. Zheng, A. Kumamoto, Y. Qian, Y. Sato, M. Liu, D. Tang, D. Gokhale *et al.*, Science **367**, 537 (2020).

[69] S. Matsushita, K. Otsuka, T. Sugihara, G. Zhu, K. Kittipaisalsilpa, M. Lee, R. Xiang, S. Chiashi, and S. Maruyama, ACS Appl. Mater. Interfaces **15**, 10965 (2023).